



Equivalent low-order angular flux nonlinear finite difference equation of MOC transport calculation

Li-Xun Liu^{1,2} · Chen Hao¹ · Yun-Lin Xu³

Received: 24 July 2020 / Revised: 13 October 2020 / Accepted: 16 October 2020 / Published online: 7 December 2020
© China Science Publishing & Media Ltd. (Science Press), Shanghai Institute of Applied Physics, the Chinese Academy of Sciences, Chinese Nuclear Society and Springer Nature Singapore Pte Ltd. 2020

Abstract The key issue in accelerating method of characteristics (MOC) transport calculations is in obtaining a completely equivalent low-order neutron transport or diffusion equation. Herein, an equivalent low-order angular flux nonlinear finite difference equation is proposed for MOC transport calculations. This method comprises three essential features: (1) the even parity discrete ordinates method is used to build a low-order angular flux nonlinear finite difference equation, and different boundary condition treatments are proposed; (2) two new defined factors, i.e., the even parity discontinuity factor and odd parity discontinuity factor, are strictly defined to achieve equivalence between the low-order angular flux nonlinear finite difference method and MOC transport calculation; (3) the energy group and angle are decoupled to construct a symmetric linear system that is much easier to solve. The equivalence of this low-order angular flux nonlinear finite difference equation is analyzed for two-dimensional (2D) pin, 2D assembly, and 2D C5G7 benchmark problems. Numerical results demonstrate that a low-order angular flux nonlinear finite difference equation that is completely

equivalent to the pin-resolved transport equation is established.

Keywords Angular flux · Equivalence · Even parity discrete ordinates method · Nonlinear finite difference

1 Introduction

Significant advances in high-performance computing clusters (HPCs) have enabled three-dimensional (3D) whole-core high-fidelity heterogeneous transport simulations at the subpin level. This is becoming increasingly important for improving the reactor performance and safety as well as providing an efficient tool for more complex and novel designs. A numerical simulation method for solving the neutron transport equation, i.e., the method of characteristics (MOC), has garnered significant attention in whole-core high-fidelity simulations as the MOC can be applied to obtain detailed flux distributions without any restrictions on the geometry mesh. Hence, efficient performances can be achieved on various HPC systems. In fact, many famous high-fidelity neutron transport simulation codes were developed based on the MOC and have been used successfully in practical reactor applications, such as the CRX code [1], DeCART code [2, 3], nTRACER [4], MPACT [5], NECP-X [6], and STREAM [7].

However, the computational feasibility of whole-core MOC calculation depends on the acceleration technique used. The neutron transport equation contains seven independent variables associated with space, angle, energy, and time. The key to accelerating high-fidelity transport calculations is to establish a low-order equivalent equation relevant to the space, angle, energy, or time while

This work was supported by the National Key R&D Program of China (No. 2018YFE0180900).

✉ Chen Hao
haochen.heu@163.com

¹ Fundamental Science On Nuclear Safety and Simulation Technology Laboratory, Harbin Engineering University, Harbin 150001, China

² Institute of Nuclear and New Energy Technology (INET), Tsinghua University, Beijing 100084, China

³ Purdue University, West Lafayette, IN 47907, USA

minimizing the computational cost. However, previous studies focused more on space and energy accelerations. An equivalent low-order equation relevant to a coarse mesh or a coarse energy interval has been established to accelerate high-order transport calculations. The coarse mesh finite difference (CMFD) method is a popular method, and different types of CMFD methods [8–15] are widely utilized to accelerate MOC calculations. Furthermore, researchers have proposed a transient multilevel (TML) method to reduce the number of high-order transport calculations significantly [16, 17]. Using the TML method, acceleration was achieved on the time scale; in this regard, large time steps were used for the MOC calculations, whereas small time steps were used for the low-order CMFD and point kinetics equations.

In the high-fidelity core simulators established, the pin-homogenized multigroup CMFD (MG CMFD) method is widely used to accelerate the convergence of pin-resolved whole-core transport calculations. Excellent acceleration has been achieved. However, the MG CMFD method only updates the scalar flux and eigenvalue, and a bottleneck is encountered. Therefore, the MOC iterations will be reduced. Subsequently, the number of iterations cannot continue to decrease if only the MG CMFD is used for acceleration. In this case, the MOC calculations still incur a significant computational burden. Therefore, whole core pin-resolved MOC calculations require a more efficient acceleration technique. Fourier analysis [18, 19] is a standard technique regularly used to investigate the stability of CMFD acceleration. Based on the Fourier analysis, the MG CMFD which based on flat source region or finer mesh can be used to further reduce the number of MOC iterations. Another potential acceleration technique is to directly update the incident angular flux and sources to further reduce the iterations of MOC calculations. Hence, an equivalent angular flux nonlinear finite difference (ANFD) equation must be established and applied to accelerate the MOC calculations. Furthermore, the domain decomposition technique is typically utilized for parallel computations, and the reactor core can be categorized into subdomains. Subsequently, the incident angular flux of each domain can be updated in time.

However, the angular flux acceleration technique has not yet been investigated; hence, we will attempt to establish an equivalent ANFD equation in this study. The even parity discrete ordinates method can be used to derive a low-order angular flux nonlinear finite difference equation. However, ensuring the equivalence between this low-order equation and the high-order pin-resolved transport equation results in new challenges. The introduction of discontinuity factors used in popular CMFD methods is a good concept. Through the strict definition and calculation of even parity and odd parity discontinuity factors based on

flux information obtained from MOC calculations, a completely equivalent angular flux nonlinear finite difference equation can be established. As relevant studies have not yet been performed, more details regarding the angular flux nonlinear finite difference equation based on the even parity discrete ordinates method, as well as the definition and calculation scheme of even and odd parity discontinuity factors including details for addressing different boundary conditions are discussed herein. Furthermore, an equivalent angular flux nonlinear finite difference equation with the pin-resolved transport equation was established in this study.

This paper is organized as follows. In Sect. 2, we provide the necessary theory for establishing the equivalent low-order angular flux nonlinear finite difference equation. The numerical method to solve this equation is discussed in Sect. 3. A code based on this new method is developed, and two-dimensional (2D) pin, 2D assembly, and 2D C5G7 benchmark problems [20] are selected to verify the equivalence of the angular flux nonlinear finite difference method. The numerical results are discussed in Sect. 4, and important conclusions are provided. Section 5 presents the summary and conclusions.

2 Methodology of angular flux nonlinear finite difference equation

2.1 Even parity discrete ordinates method for neutron transport equation

To provide a detailed description of the angular flux nonlinear finite difference equation, we begin with the multigroup neutron transport equation in the Cartesian coordinate system, as follows:

$$\boldsymbol{\Omega} \cdot \nabla \psi_g(\mathbf{r}, \boldsymbol{\Omega}) + \Sigma_{t,g}(\mathbf{r}) \psi_g(\mathbf{r}, \boldsymbol{\Omega}) = S_g(\mathbf{r}, \boldsymbol{\Omega}), \quad (1)$$

where vector \mathbf{r} is the spatial position relative to the reference point, and vector $\boldsymbol{\Omega}$ is the unit direction of flying with respect to the reference. Subscript g denotes the energy group index using multigroup approximation. This equation can represent the steady-state or transient neutron transport equation. When it represents a transient equation, the time variable is eliminated for brevity, as follows:

$$S_g(\mathbf{r}, \boldsymbol{\Omega}) = -\frac{1}{v} \frac{\partial}{\partial t} \psi_g(\mathbf{r}, \boldsymbol{\Omega}) + S_{s,g}(\mathbf{r}, \boldsymbol{\Omega}) + \frac{1}{4\pi} S_{f,g}(\mathbf{r}) + \frac{1}{4\pi} S_{d,g}(\mathbf{r}) + S_{e,g}(\mathbf{r}, \boldsymbol{\Omega}), \quad (2a)$$

where S_s , S_f , S_d , and S_e are the scattering, fission, delayed, and external sources, respectively. The external source is often disregarded, except when it must be considered. The fission and delayed neutron sources are isotropic. For the

steady state, the time derivative term is zero, and the delayed neutron source is included in the fission source. If we discretize the time derivative term $\frac{\partial}{\partial t} \psi_g(\mathbf{r}, \boldsymbol{\Omega})$ with fluxes at the current and last time steps, the transient equation will become a transient fixed source equation, which can be solved in a manner similar to the steady-state equation. Therefore, we will only discuss the steady-state equation, and Eq. (2a) can be expressed as follows:

$$S_g(\mathbf{r}, \boldsymbol{\Omega}) = S_{s,g}(\mathbf{r}, \boldsymbol{\Omega}) + \frac{1}{4\pi} S_{f,g}(\mathbf{r}). \tag{2b}$$

The scattering and fission source can be expressed in terms of the angular flux as follows:

$$S_{s,g}(\mathbf{r}, \boldsymbol{\Omega}) = \sum_{g'} \int_{4\pi} \psi_{g'}(\mathbf{r}, \boldsymbol{\Omega}') \Sigma_{s,g'g}(\mathbf{r}, \mu_0) d\boldsymbol{\Omega}', \tag{2c}$$

$$S_{f,g}(\mathbf{r}) = \frac{\chi_g}{k_{\text{eff}}} \sum_{g'} v \Sigma_f(\mathbf{r}) \phi_{g'}(\mathbf{r}), \tag{2d}$$

where ψ , ϕ , Σ , χ , μ_0 , and k_{eff} are the angular flux, scalar flux, macro-cross sections, fission spectrum, cosine of scattering angle in the center of mass system, and eigenvalue with a standard definition in nuclear reactor physics, respectively. Using the discrete ordinates method, we can represent the angular space with selected angles as follows:

$$\phi_g(\mathbf{r}) = \int_{4\pi} \psi_g(\mathbf{r}, \boldsymbol{\Omega}) d\boldsymbol{\Omega} = \sum_{i=1}^M \omega_i \psi_{g,i}(\mathbf{r}), \tag{3}$$

where $\boldsymbol{\Omega}_i$ and ω_i are the selected angles and weights, respectively, and are known as the S_N quadrature set; M is the total number of discrete directions. Here, we use subscript i to represent quantities at angle $\boldsymbol{\Omega}_i$ and subscript $-i$ to represent quantities at angle $-\boldsymbol{\Omega}_i$. The equations for angular fluxes in opposite directions are as follows:

$$\boldsymbol{\Omega}_i \cdot \nabla \psi_{g,i}(\mathbf{r}) + \Sigma_{t,g}(\mathbf{r}) \psi_{g,i}(\mathbf{r}) = S_{g,i}(\mathbf{r}), \tag{4a}$$

$$-\boldsymbol{\Omega}_i \cdot \nabla \psi_{g,-i}(\mathbf{r}) + \Sigma_{t,g}(\mathbf{r}) \psi_{g,-i}(\mathbf{r}) = S_{g,-i}(\mathbf{r}). \tag{4b}$$

The even and odd parity fluxes are expressed as follows:

$$\psi_{g,i}^+(\mathbf{r}) = [\psi_{g,i}(\mathbf{r}) + \psi_{g,-i}(\mathbf{r})]/2, \tag{5a}$$

$$\psi_{g,i}^-(\mathbf{r}) = [\psi_{g,i}(\mathbf{r}) - \psi_{g,-i}(\mathbf{r})]/2. \tag{5b}$$

The even and odd parity fluxes exhibit the following properties:

$$\psi_{g,i}^+(\mathbf{r}) = \psi_{g,-i}^+(\mathbf{r}), \tag{6a}$$

$$\psi_{g,i}^-(\mathbf{r}) = -\psi_{g,-i}^-(\mathbf{r}). \tag{6b}$$

Using Eqs. (4) and (5), we can obtain the even and odd parity transport equations as follows:

$$\boldsymbol{\Omega}_i \cdot \nabla \psi_{g,i}^-(\mathbf{r}) + \Sigma_{t,g}(\mathbf{r}) \psi_{g,i}^+(\mathbf{r}) = S_{g,i}^+(\mathbf{r}), \tag{7a}$$

$$\boldsymbol{\Omega}_i \cdot \nabla \psi_{g,i}^+(\mathbf{r}) + \Sigma_{t,g}(\mathbf{r}) \psi_{g,i}^-(\mathbf{r}) = S_{g,i}^-(\mathbf{r}), \tag{7b}$$

where $S_{g,i}^+(\mathbf{r})$ and $S_{g,i}^-(\mathbf{r})$ are the even and odd parity sources, respectively, expressed as

$$S_{g,i}^+(\mathbf{r}) = [S_{g,i}(\mathbf{r}) + S_{g,-i}(\mathbf{r})]/2, \tag{8a}$$

$$S_{g,i}^-(\mathbf{r}) = [S_{g,i}(\mathbf{r}) - S_{g,-i}(\mathbf{r})]/2. \tag{8b}$$

As the fission sources are isotropic, we have

$$S_{g,i}^+(\mathbf{r}) = S_{s,g,i}^+(\mathbf{r}) + \frac{1}{4\pi} S_{f,g}(\mathbf{r}), \tag{9a}$$

$$S_{g,i}^-(\mathbf{r}) = S_{s,g,i}^-(\mathbf{r}), \tag{9b}$$

where $S_{s,g,i}^+(\mathbf{r})$ and $S_{s,g,i}^-(\mathbf{r})$ are the even and odd parity scattering sources, expressed as

$$S_{s,g,i}^+(\mathbf{r}) = [S_{s,g,i}(\mathbf{r}) + S_{s,g,-i}(\mathbf{r})]/2, \tag{10a}$$

$$S_{s,g,i}^-(\mathbf{r}) = [S_{s,g,i}(\mathbf{r}) - S_{s,g,-i}(\mathbf{r})]/2. \tag{10b}$$

Here, $S_{s,g,i}(\mathbf{r})$ is the angle-dependent scattering source, expressed as

$$S_{s,g,i}(\mathbf{r}) = \sum_{g'} \int_{4\pi} \psi_{g'}(\mathbf{r}, \boldsymbol{\Omega}') \Sigma_{s,g'g}(\mathbf{r}, \mu_0) d\boldsymbol{\Omega}'. \tag{11}$$

μ_0 is the cosine of the scattering angle in the center of mass system, where $\mu_0 = \boldsymbol{\Omega} \cdot \boldsymbol{\Omega}'$. With a P_n expansion of the scattering cross sections, we obtain

$$\Sigma_{s,g'g}(\mathbf{r}, \mu_0) = \sum_{k=0}^{\infty} \frac{2k+1}{4\pi} \Sigma_{s,k,g'g}(\mathbf{r}) P_k(\mu_0), \tag{12}$$

where P_k are the Legendre polynomials and $\Sigma_{s,k}$ are P_k scattering moments. By expanding the even and odd parity scattering sources with a P_0 expansion, we have

$$S_{s,g,i}^+(\mathbf{r}) = \frac{1}{4\pi} \sum_{g'} \Sigma_{s,g'g}(\mathbf{r}) \sum_{i'} \omega_{i'} \psi_{g',i'}(\mathbf{r}), \tag{13a}$$

$$S_{s,g,i}^-(\mathbf{r}) = 0. \tag{13b}$$

Combined with Eqs. (9) and (13), the even and odd parity sources can be expressed as follows:

$$S_{g,i}^+(\mathbf{r}) = \frac{1}{4\pi} \sum_{g'} \Sigma_{s,g'g}(\mathbf{r}) \sum_{i'} \omega_{i'} \psi_{g',i'}^+(\mathbf{r}) + \frac{1}{4\pi} \frac{\chi_g}{k_{\text{eff}}} \sum_{g'} v \Sigma_{f,g'}(\mathbf{r}) \sum_{i'} \omega_{i'} \psi_{g',i'}^+(\mathbf{r}), \tag{14a}$$

$$S_{g,i}^-(\mathbf{r}) = 0. \tag{14b}$$

Integrate the even parity transport equation in Eq. (7a) over a region with constant a cross section as follows:

$$\iint_{\Gamma} \psi_{g,i}^-(\mathbf{r}) \boldsymbol{\Omega}_i \cdot \hat{\mathbf{n}} d\Gamma + V_r \Sigma_{t,g,i,r} \bar{\psi}_{g,i,r}^+ = V_r \bar{S}_{g,i,r}^+ \tag{15}$$

where subscript r is the region index; V_r is the volume of region r ; Γ is the surface of region r ; $\hat{\mathbf{n}}$ is the unit normal direction vector of the surface; $\bar{\psi}_{g,i,r}^+$ and $\bar{S}_{g,i,r}^+$ are the node average even parity flux and node average even parity source weighted by the region volume, respectively. $\Sigma_{t,g,i,r}$ is the angle-dependent total macro-cross section, defined as follows:

$$\Sigma_{t,g,i,r} = \frac{\int_V \Sigma_{t,g}(\mathbf{r}) \psi_{g,i}^+(\mathbf{r}) dV}{\int_V \psi_{g,i}^+(\mathbf{r}) dV} \tag{16}$$

It is noteworthy that the divergence theorem was used for deriving Eq. (15).

$$\nabla \cdot (\psi_{g,i}^-(\mathbf{r}) \boldsymbol{\Omega}_i) = \boldsymbol{\Omega}_i \cdot \nabla \psi_{g,i}^-(\mathbf{r}) + \psi_{g,i}^- \nabla \cdot \boldsymbol{\Omega}_i = \boldsymbol{\Omega}_i \cdot \nabla \psi_{g,i}^-(\mathbf{r}), \tag{17a}$$

$$\iint_{\Gamma} \psi_{g,i}^-(\mathbf{r}) \boldsymbol{\Omega}_i \cdot \hat{\mathbf{n}} d\Gamma = \iiint_V \nabla \cdot (\psi_{g,i}^-(\mathbf{r}) \boldsymbol{\Omega}_i) dV = \iiint_V \boldsymbol{\Omega}_i \cdot \nabla \psi_{g,i}^-(\mathbf{r}) dV. \tag{17b}$$

The surface of region r is divided into n_r segments, where n_r is the number of neighbors. Each segment is the interface between region r and one of its neighbors. Define the average odd parity flux on each segment as follows:

$$\bar{\psi}_{g,i,r}^- = \frac{1}{A_{i,r,m}} \iint_{\Gamma_m} \psi_{g,i}^-(\mathbf{r}) \boldsymbol{\Omega}_i \cdot \hat{\mathbf{n}} d\Gamma, \tag{18a}$$

$$A_{i,r,m} = \iint_{\Gamma_m} |\boldsymbol{\Omega}_i \cdot \hat{\mathbf{n}}| d\Gamma, \tag{18b}$$

where n is the neighbor node of node r , and Γ_m is the interface between r and n . The average odd parity flux on the surface can represent the net number of neutrons passing through the interface in a certain direction, and it exhibits the following property:

$$\bar{\psi}_{g,i,r}^- = -\bar{\psi}_{g,-i,r}^- \tag{19}$$

By rearranging Eq. (15), we can obtain the even parity flux equation as follows:

$$\sum_{n \in \text{neighbors}} A_{i,r,m} \bar{\psi}_{g,i,m}^- + V_r \Sigma_{t,g,i,r} \bar{\psi}_{g,i,r}^+ = V_r \bar{S}_{g,i,r}^+ \tag{20}$$

The even parity flux equation exactly preserves the neutron balance in each direction and in each coarse mesh. If the relationship between the average odd parity flux $\bar{\psi}_{g,i,r}^-$ and the node average even parity flux $\bar{\psi}_{g,i,r}^+$ is obtained, then Eq. (20) can be solved further. This relationship can be obtained from the odd parity transport equation.

Integrating the odd parity transport equation (Eq. (7b)) over each segment of the surface, we obtain

$$\iint_{\Gamma_m} \boldsymbol{\Omega}_i \cdot \nabla \psi_{g,i}^+(\mathbf{r}) \boldsymbol{\Omega}_i \cdot \hat{\mathbf{n}} d\Gamma + A_{i,r,m} \Sigma_{t,g,i,r} \bar{\psi}_{g,i,m}^- = 0. \tag{21}$$

The left hand of Eq. (21) is the average derivative of the even parity flux on interface Γ_m in the $\boldsymbol{\Omega}_i$ direction and can be defined as follows:

$$\bar{\psi}_{g,i,m}'^+ = \frac{1}{A_{i,r,m}} \iint_{\Gamma_m} \boldsymbol{\Omega}_i \cdot \nabla \psi_{g,i}^+(\mathbf{r}) \boldsymbol{\Omega}_i \cdot \hat{\mathbf{n}} d\Gamma. \tag{22}$$

Substituting Eq. (22) into Eq. (21), we have

$$\bar{\psi}_{g,i,m}'^+ = -\Sigma_{t,g,i,r} \bar{\psi}_{g,i,m}^- \tag{23}$$

Through a finite difference approximation for $\bar{\psi}_{g,i,m}'^+$, we obtain the following odd parity flux equation:

$$\frac{\bar{\psi}_{g,i,m}^- - \bar{\psi}_{g,i,r}^+}{h_{i,r,m}} \approx -\Sigma_{t,g,i,r} \bar{\psi}_{g,i,m}^- \tag{24}$$

where $\bar{\psi}_{g,i,m}^+$ is the average even parity flux on the surface between r and n , and $h_{i,r,m}$ is the thickness of the node center to the surface center in the direction of angle $\boldsymbol{\Omega}_i$.

$$\bar{\psi}_{g,i,m}^+ = \frac{1}{A_{i,r,m}} \iint_{\Gamma_m} \psi_{g,i}^+(\mathbf{r}) |\boldsymbol{\Omega}_i \cdot \hat{\mathbf{n}}| d\Gamma, \tag{25a}$$

$$h_{i,r,m} = \left| \frac{\iint_{\Gamma_m} (\mathbf{r} \cdot \boldsymbol{\Omega}_i) |\boldsymbol{\Omega}_i \cdot \hat{\mathbf{n}}| d\Gamma}{\iint_{\Gamma_m} |\boldsymbol{\Omega}_i \cdot \hat{\mathbf{n}}| d\Gamma} - \frac{\int_V \mathbf{r} \cdot \boldsymbol{\Omega}_i dV}{\int_V dV} \right|. \tag{25b}$$

The average even parity flux on the surface exhibits following priority:

$$\bar{\psi}_{g,i,m}^+ = \bar{\psi}_{g,-i,m}^+ \tag{26}$$

2.2 Definition and application of discontinuity factor

To render all $\bar{\psi}_{g,i,r}^+$, $\bar{\psi}_{g,i,m}^+$ and $\bar{\psi}_{g,i,m}^-$ in the odd parity flux equation (Eq. (24)) satisfy the MOC transport calculation, we introduced a factor known as the even parity discontinuity factor, $f_{g,i,m}^+$, as follows:

$$f_{g,i,m}^+ = \frac{\bar{\psi}_{g,i,m}^+}{\left(\bar{\psi}_{g,i,r}^+ - h_{i,r,m} \Sigma_{t,g,i,r} \bar{\psi}_{g,i,m}^- \right)}, \tag{27}$$

$f_{g,i,m}^+$ will be greater than zero when the denominator of Eq. (27) is positive. However, the denominator can less than or equal to zero. In this case, $f_{g,i,m}^+$ will be infinite or negative. To avoid this, we introduced another discontinuity factor to Eq. (27), i.e., the odd parity discontinuity factor, $f_{g,i,m}^-$.

$$f_{g,i,r}^+ = \frac{\bar{\psi}_{g,i,r}^+}{\left(\bar{\psi}_{g,i,r}^+ - h_{i,m} \frac{\Sigma_{t,g,i,r}}{f_{g,i,m}^-} \bar{\psi}_{g,i,r}^-\right)} \tag{28}$$

An algorithm was designed to determine the even and odd parity discontinuity factors. This algorithm begins by evaluating the following conditional:

$$\bar{\psi}_{g,i,r}^+ - h_{i,m} \Sigma_{t,g,i,r} \bar{\psi}_{g,i,r}^- > \bar{\psi}_{g,i,r}^+ \tag{29}$$

If the condition in Eq. (29) is true, then the even and odd parity discontinuity factors can be calculated from the MOC solutions as follows:

$$f_{g,i,m}^+ = \frac{\bar{\psi}_{g,i,m}^+}{\bar{\psi}_{g,i,r}^+ - h_{i,m} \Sigma_{t,g,i,r} \bar{\psi}_{g,i,r}^-}, \tag{30a}$$

$$f_{g,i,m}^- = 1. \tag{30b}$$

If the condition is false, then different equations are designed to calculate the even and odd parity discontinuity factors as follows:

$$f_{g,i,m}^+ = \frac{\bar{\psi}_{g,i,m}^+ + h_{i,m} \Sigma_{t,g,i,r} \bar{\psi}_{g,i,r}^-}{\bar{\psi}_{g,i,r}^+}, \tag{31a}$$

$$f_{g,i,m}^- = f_{g,i,m}^+. \tag{31b}$$

Using this approach, the even and odd parity discontinuity factors will be positive at all times. Rearranging Eq. (28) yields

$$\frac{\bar{\psi}_{g,i,m}^+}{f_{g,i,m}^+} + h_{i,m} \frac{\Sigma_{t,g,i,r}}{f_{g,i,m}^-} \bar{\psi}_{g,i,r}^- = \bar{\psi}_{g,i,r}^+ \tag{32}$$

If neighbor node n is within the computational domain, then a similar equation is obtained for the other side of the interface Γ_m , as follows:

$$\frac{\bar{\psi}_{g,i,nr}^+}{f_{g,i,nr}^+} + h_{i,nr} \frac{\Sigma_{t,g,i,n}}{f_{g,i,nr}^-} \bar{\psi}_{g,i,nr}^- = \bar{\psi}_{g,i,n}^+ \tag{33}$$

Combining Eqs. (32) and (33) and the continuity condition $\bar{\psi}_{g,i,m}^+ = \bar{\psi}_{g,i,nr}^+$, $\bar{\psi}_{g,i,r}^- = -\bar{\psi}_{g,i,nr}^-$, we obtain

$$\left(f_{g,i,m}^+ h_{i,m} \frac{\Sigma_{t,g,i,r}}{f_{g,i,m}^-} + f_{g,i,nr}^+ h_{i,nr} \frac{\Sigma_{t,g,i,n}}{f_{g,i,nr}^-} \right) \bar{\psi}_{g,i,r}^- = f_{g,i,m}^+ \bar{\psi}_{g,i,r}^+ - f_{g,i,nr}^+ \bar{\psi}_{g,i,n}^+ \tag{34}$$

As for the vacuum boundary surface, the incident angular flux is zero. Therefore, we have the equation $\bar{\psi}_{g,i,m}^- = \bar{\psi}_{g,i,m}^+$, which can be derived from Eqs. (18a) and (25a). Combining this equation with Eq. (32), we obtain

$$\left(f_{g,i,m}^+ h_{i,m} \frac{\Sigma_{t,g,i,r}}{f_{g,i,m}^-} + 1 \right) \bar{\psi}_{g,i,m}^- = f_{g,i,m}^+ \bar{\psi}_{g,i,r}^+ \tag{35}$$

For the reflective boundary surface, the angular fluxes in the reflect directions are equal. Therefore, we have the continuity condition $\bar{\psi}_{g,i,m}^+ = \bar{\psi}_{g,i^*,m}^+$ and $\bar{\psi}_{g,i,m}^- = -\bar{\psi}_{g,i^*,m}^-$, where subscript i^* and i represent a pair of angles in the incident and reflective directions, respectively. Figure 1 shows an illustration of the reflective boundary condition.

Combined with Eq. (32) for both the angle i and i^* , we obtain

$$\left(f_{g,i,m}^+ h_{i,m} \frac{\Sigma_{t,g,i,r}}{f_{g,i,m}^-} + f_{g,i^*,m}^+ h_{i^*,m} \frac{\Sigma_{t,g,i^*,r}}{f_{g,i^*,m}^-} \right) \bar{\psi}_{g,i,m}^- = f_{g,i,m}^+ \bar{\psi}_{g,i,r}^+ - f_{g,i^*,m}^+ \bar{\psi}_{g,i^*,r}^+ \tag{36}$$

In general, the relationships between the surface average odd parity flux and node average even parity flux for both the interior surface and boundary surface are established through Eqs. (34), (35), and (36). Moreover, these equations satisfy the high-order MOC solution through the strict definitions of the even and odd parity discontinuity factors.

2.3 Construction of angular flux nonlinear finite difference linear system

Based on Eqs. (34), (35), and (36), the odd parity fluxes on the interior and boundary surfaces can be expressed as a linear function of the neighbor average even parity fluxes using the coupling coefficient C .

For the interior surface, we have

$$\bar{\psi}_{g,i,m}^- = C_{g,i,m} \bar{\psi}_{g,i,r}^+ - C_{g,i,nr} \bar{\psi}_{g,i,n}^+, \tag{37a}$$

where

$$C_{g,i,m} = \frac{f_{g,i,m}^+}{\left(f_{g,i,m}^+ h_{i,m} \frac{\Sigma_{t,g,i,r}}{f_{g,i,m}^-} + f_{g,i,nr}^+ h_{i,nr} \frac{\Sigma_{t,g,i,n}}{f_{g,i,nr}^-} \right)}, \tag{37b}$$

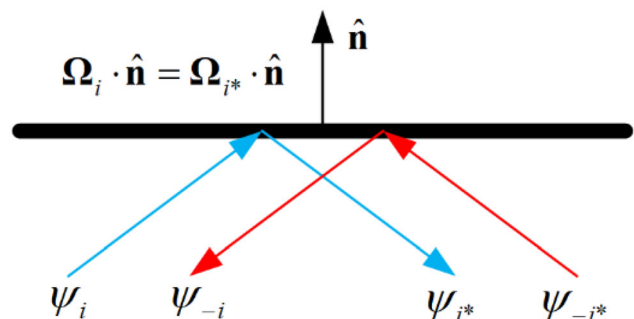


Fig. 1 (Color online) Illustration of reflective boundary condition

$$C_{g,i,nr} = \frac{f_{g,i,nr}^+}{\left(f_{g,i,m}^+ h_{i,m} \frac{\Sigma_{t,g,i,r}}{f_{g,i,m}^-} + f_{g,i,nr}^+ h_{i,nr} \frac{\Sigma_{t,g,i,n}}{f_{g,i,nr}^-}\right)}. \tag{37c}$$

For the vacuum boundary surface, we have

$$\bar{\psi}_{g,i,m}^- = C_{g,i,m} \bar{\psi}_{g,i,r}^+ \tag{38a}$$

where

$$C_{g,i,m} = \frac{f_{g,i,m}^+}{\left(f_{g,i,m}^+ h_{i,m} \frac{\Sigma_{t,g,i,r}}{f_{g,i,m}^-} + 1\right)}. \tag{38b}$$

For the reflective boundary surface, we have

$$\bar{\psi}_{g,i,m}^- = C_{g,i,m} \bar{\psi}_{g,i,r}^+ - C_{g,i^*,m} \bar{\psi}_{g,i^*,r}^+ \tag{39a}$$

where

$$C_{g,i,m} = \frac{f_{g,i,m}^+}{\left(f_{g,i,m}^+ h_{i,m} \frac{\Sigma_{t,g,i,r}}{f_{g,i,m}^-} + f_{g,i^*,m}^+ h_{i^*,m} \frac{\Sigma_{t,g,i^*,r}}{f_{g,i^*,m}^-}\right)}, \tag{39b}$$

$$C_{g,i^*,m} = \frac{f_{g,i^*,m}^+}{\left(f_{g,i,m}^+ h_{i,m} \frac{\Sigma_{t,g,i,r}}{f_{g,i,m}^-} + f_{g,i^*,m}^+ h_{i^*,m} \frac{\Sigma_{t,g,i^*,r}}{f_{g,i^*,m}^-}\right)}. \tag{39c}$$

Substituting Eqs. (37)–(39) into Eq. (20), we obtain the following angular flux nonlinear difference linear system:

$$\sum_{n \in \text{neighbors}} A_{i,m} \left(C_{g,i,m} \bar{\psi}_{g,i,r}^+ - C_{g,i,nr} \bar{\psi}_{g,i,n}^+ \right) + V_r \Sigma_{t,g,i,r} \bar{\psi}_{g,i,r}^+ = b_{g,i,r}. \tag{40}$$

If the homogenized cross sections and coupling coefficients are obtained from the results of the MOC transport calculation, then the ANFD linear system can be solved. As the even parity fluxes in opposite directions are equal, only the ANFD linear system need to be solved on a half-angular space.

3 Solving angular flux nonlinear difference equation

To solve the angular flux nonlinear difference equation, different solving strategies for decoupling the energy group and angle are proposed herein. If the scattering sources are determined simultaneously with the even parity fluxes, then all groups and all angles are coupled together. The terms on the right side of the linear system can be expressed as follows:

$$b_{g,i,r} = V_r \frac{1}{k_{\text{eff}}} \frac{\chi_g}{4\pi} \sum_{g'} v \bar{\Sigma}_{t,g',r} \sum_{i'} \omega_{i'} \bar{\psi}_{g',i',r}^+ \tag{41a}$$

If all scattering sources other than the in-group scattering term are provided, then all angles are coupled together, and the linear system can still be solved by group separately, as follows:

$$b_{g,i,r} = V_r \frac{1}{k_{\text{eff}}} \frac{\chi_g}{4\pi} \sum_{g'} v \bar{\Sigma}_{t,g',r} \sum_{i'} \omega_{i'} \bar{\psi}_{g',i',r}^+ + V_r \frac{1}{4\pi} \sum_{g' \neq g} \bar{\Sigma}_{s,g',g,r} \sum_{i'} \omega_{i'} \bar{\psi}_{g,i',r}^+ \tag{41b}$$

If the scattering sources are all treated as specified, then the linear system can be solved by group and angle separately, as follows:

$$b_{g,i,r} = V_r \frac{1}{k_{\text{eff}}} \frac{\chi_g}{4\pi} \sum_{g'} v \bar{\Sigma}_{t,g',r} \sum_{i'} \omega_{i'} \bar{\psi}_{g',i',r}^+ + V_r \frac{1}{4\pi} \sum_{g'} \bar{\Sigma}_{s,g',g,r} \sum_{i'} \omega_{i'} \bar{\psi}_{g',i',r}^+ + A_{i,m} C_{g,i^*,m} \bar{\psi}_{g,i^*,r}^+ \tag{41c}$$

It is noteworthy that the last term in Eq. (41c) appears only when a reflect boundary condition exists on the node surface.

3.1 Decoupling of energy group and angle

To solve the linear system by group and angle separately, we would like to keep $C_{g,i,m} = C_{g,i,nr}$ in the interior surfaces such that the linear system will be symmetric. A symmetric linear system is much easier to solve than an asymmetric system. To create a symmetric ANFD linear system, the coupling coefficients for the interior surface are redefined as follows:

$$\bar{\psi}_{g,i,m}^- = C_{g,i,m} \left(\bar{\psi}_{g,i,r}^+ - \bar{\psi}_{g,i,n}^+ \right) - \psi_{g,i,m}, \tag{42a}$$

$$C_{g,i,m} = C_{g,i,nr} = \frac{f_{g,i,m}^+ + f_{g,i,nr}^+}{\left(f_{g,i,m}^+ h_{i,m} \frac{\Sigma_{t,g,i,r}}{f_{g,i,m}^-} + f_{g,i,nr}^+ h_{i,nr} \frac{\Sigma_{t,g,i,n}}{f_{g,i,nr}^-} \right)}, \tag{42b}$$

$$\psi_{g,i,m} = \frac{f_{g,i,nr}^+ \bar{\psi}_{g,i,r}^+ - f_{g,i,m}^+ \bar{\psi}_{g,i,n}^+}{\left(f_{g,i,m}^+ h_{i,m} \frac{\Sigma_{t,g,i,r}}{f_{g,i,m}^-} + f_{g,i,nr}^+ h_{i,nr} \frac{\Sigma_{t,g,i,n}}{f_{g,i,nr}^-} \right)}, \tag{42c}$$

where $\psi_{g,i,m}$ is the asymmetric term of Eq. (42a), which can be determined using even parity fluxes. Substituting Eq. (42) into Eq. (40) and placing the asymmetric term to the right side of the equation, the ANFD linear system is rearranged as follows:

$$\begin{aligned}
 & \left[\begin{aligned} & \left(A_{i,rN} C_{g,i,rN} + A_{i,rS} C_{g,i,rS} + A_{i,rW} C_{g,i,rW} \right) + V_r \bar{\Sigma}_{t,g,i,r} \end{aligned} \right] \bar{\psi}_{g,i,r}^{+k} \\
 & - \left(\begin{aligned} & A_{i,Nr} C_{g,i,Nr} \bar{\psi}_{g,i,N}^{+k} + A_{i, Sr} C_{g,i, Sr} \bar{\psi}_{g,i, S}^{+k} + A_{i, Wr} C_{g,i, Wr} \bar{\psi}_{g,i, W}^{+k} \\ & + A_{i, Er} C_{g,i, Er} \bar{\psi}_{g,i, E}^{+k} + A_{i, Br} C_{g,i, Br} \bar{\psi}_{g,i, B}^{+k} + A_{i, Tr} C_{g,i, Tr} \bar{\psi}_{g,i, T}^{+k} \end{aligned} \right) , \\
 & = V_r \frac{1}{k_{eff}} \frac{\chi_g}{4\pi} \sum_{g'} v \bar{\Sigma}_{f, g', r} \sum_{i'} \omega_i \bar{\psi}_{g', i', r}^{+k-1} + V_r \frac{1}{4\pi} \sum_{g'} \bar{\Sigma}_{s, g', r} \sum_{i'} \omega_i \bar{\psi}_{g', i', r}^{+k-1} \\
 & + A_{i, rn} C_{g, i^*, rn} \bar{\psi}_{g, i^*, r}^{+k-1} + A_{i, rn} \chi_{g, i, rn}^{k-1}
 \end{aligned}$$

where $N, S, W, E, T,$ and B represent the north, south, west, east, top, and bottom surfaces of the node, respectively. The superscript k denotes the power iteration number. As the symmetric and diagonal dominant matrix is a symmetric positive definite matrix, Eq. (43) will become an expression for a symmetric positive definite linear system. Furthermore, the preconditioned conjugate gradient (CG) method [21] can be used to solve this linear system.

It is noteworthy that decoupling the angle and energy group will increase the iteration number of the ANFD method. However, the ANFD computing costs are low compared with those of MOC calculations, and they can be reduced significantly using the multilevel acceleration method, which has been implemented in several established core simulators [22–24]. The main idea of the multilevel acceleration method is to use a few-group CMFD linear system, such as a one- or two-group CMFD, to reduce the computing burden of the MG CMFD linear system. The few-group CMFD linear system is used to provide an effective estimation of the eigenvalue at the beginning of each power iteration, thereby significantly reducing the outer iteration number of the MG CMFD linear system. Therefore, a new approach similar to the multilevel acceleration method can be used to reduce the iteration number of ANFD required for convergence. This will be investigated further in future studies.

Meanwhile, if we wish to solve the linear system with all angles coupled or all energy groups coupled, it would be meaningless to maintain $C_{g,i,rn} = C_{g,i,nr}$. In this case, we will define the interior surface coupling coefficients directly from Eq. (37), and the preconditioned CG method will not be used.

3.2 Preconditioned Krylov subspace method

The direct solution of this linear system is unpractical as the matrix can become highly ill-conditioned, causing problems in the numerical solution. The Krylov subspace method has been proven to be extremely effective for solving large, nonsymmetric, sparse linear systems,

particularly when a good preconditioner is applied. In this study, the right preconditioned generalized minimal residual (GMRES) method was used to solve the ANFD linear system. The right preconditioned GMRES algorithm can be summarized as follows:

Algorithm 1: Right Preconditioned GMRES

- Step 1: Compute $r_0 = b - Ax_0$, $\beta = \|r_0\|_2$, and $v_1 = r_0 / \beta$.
- Step 2: Do $j = 1, m$.
 - Step 2.1: Compute $w := AM^{-1}v_j$.
 - Step 2.2: Do $i = 1, j$.
 - Step 2.2.1: Compute $h_{i,j} := (w, v_i)$.
 - Step 2.2.2: Compute $w := w - h_{i,j}v_i$.
 - Step 2.3: End Do.
 - Step 2.4: Compute $h_{j+1,j} = \|w\|_2$ and $v_{j+1} = w / h_{j+1,j}$.
 - Step 2.5: Define $V_m := [v_1, v_2, \dots, v_m]$, $\hat{H}_m = \{h_{i,j}\}_{1 \leq i \leq j+1; 1 \leq j \leq m}$.
 - Step 2.6: Compute $y_m = \operatorname{argmin}_y \|\beta e_1 - \hat{H}_m y\|_2$.
 - Step 2.7: If $|s_{m+1}^*| \leq \varepsilon$, break.
- Step 3: End Do.
- Step 4: Compute $x_m = x_0 + M^{-1}(V_m y_m)$.

Meanwhile, if we decoupling the energy group and angle to construct a symmetric positive definite linear system, then the preconditioned conjugate gradient method can be used to solve the ANFD linear system. The left preconditioned conjugate gradient algorithm can be summarized as follows:

Algorithm 2: Left Preconditioned CG

- Step 1:* Compute $r_0 = b - Ax_0$, $z_0 = M^{-1}r_0$ and $p_0 = z_0$.
- Step 2:* Do $j = 0, 1, \dots$ until convergence.
 - Step 2.1:* Compute $\alpha_j = (r_j, z_j) / (Ap_j, p_j)$.
 - Step 2.2:* Compute $x_{j+1} = x_j + \alpha_j p_j$.
 - Step 2.3:* Compute $r_{j+1} = r_j - \alpha_j Ap_j$.
 - Step 2.4:* Compute $z_{j+1} = M^{-1}r_{j+1}$.
 - Step 2.5:* Compute $\beta_j = (r_{j+1}, z_{j+1}) / (r_j, z_j)$.
 - Step 2.6:* Compute $p_{j+1} = z_{j+1} + \beta_j p_j$.
- Step 3:* End Do.

As for precondition technology, a self-developed RSILU preconditioner has been used to improve parallel computing capability and minimize computational burden. The RSILU preconditioner does not require a multicolor ordering strategy for parallel computing and can provide convergence rates comparable to the standard incomplete lower-upper preconditioner. More details are available in the literature [25].

3.3 Iteration scheme of ANFD method

Once the node and surface angular flux obtained from the MOC calculation become available, the ANFD homogenized cross sections as well as the even and odd parity discontinuity factors can be easily obtained using Eqs. (16) and (30), respectively. The strategy of decoupling the energy group and angle was used to construct the ANFD linear system, and the coupling coefficients were calculated using Eqs. (37)–(39). Hence, an equivalent ANFD linear system can be established. It is noteworthy that the asymmetric term arising from the construction of a symmetric positive definite matrix should be updated with the even parity angular flux when solving the ANFD linear system. The right preconditioned GMRES solver was used to solve the ANFD linear system in this study. The exit from the GMRES solver to the ANFD cycle occurs when the required reduction in the relative L2-norm of the residual vector is achieved.

After solving the ANFD linear system, new even parity flux distributions and eigenvalues were obtained. To update the 2D MOC parameters, the average scalar flux on each node and the average angular flux on each surface were reconstructed as follows, indicated as $\bar{\phi}_{g,r}$ and $\bar{\psi}_{g,i,m}$, respectively:

$$\bar{\phi}_{g,r} = 2\pi \sum_{i=1}^M (w_i \bar{\psi}_{g,i,r}^+) \tag{44a}$$

$$\bar{\psi}_{g,i,m} = \frac{|\Omega_i \cdot \hat{\mathbf{n}}|}{\Omega_i \cdot \hat{\mathbf{n}}} \bar{\psi}_{g,i,m}^- + \bar{\psi}_{g,i,m}^+ \tag{44b}$$

The former was used to update the scalar flux in the flat source regions, whereas the latter was used to update the incident angular flux on the boundary surface. The M in Eq. (44a) denotes the total number of discrete directions, which is consistent with the number of MOC azimuthal angles. After updating the average node scalar flux $\bar{\phi}_{g,r}$ and average surface angular flux $\bar{\psi}_{g,i,m}$, 2D MOC calculations were performed, and the cell-averaged cross sections as well as the even and odd parity discontinuity factors were updated. Subsequently, ANFD was performed using the updated cross sections as well as the even and odd parity discontinuity factors. This process was repeated until all convergence criteria were satisfied. The iteration scheme of the ANFD method is depicted in Fig. 2.

4 Numerical results

To investigate the equivalence of the ANFD method proposed herein, a code written in the C language was developed and three different test problems were selected: 2D pin, 2D assembly, and 2D C5G7 benchmark problems. In addition, a self-defined problem was tested to compare the acceleration capabilities of ANFD and CMFD in the void region.

For all these problems, the flux convergence criterion was 10^{-5} by comparing the infinite norm of the scalar flux in the flat source region, and the eigenvalue convergence criterion was 10^{-7} . For the ray tracing parameter, a 0.01 cm ray spacing with 72 azimuthal angles and a Tabuchi–Yamamoto polar quadrature [26] with three polar angles per half-space were used for all the problems. The computer used to execute the code comprised an Inter(R) Core (TM) i5-7200U CPU @ 2.50 GHz with an 8.0G RAM. The basic computing unit for the ANFD was the pin cell.

For the 2D pin cell and 2D assembly problems, the eigenvalue and flux distribution error in the angle, energy group, and space were compared with those of the MOC calculations. In addition, three parameters were selected to assess the overall relative error of the even parity flux, i.e., the average relative error (AVG), root-mean-square of relative error (RMS), and maximum relative error (MAX), defined as follows:

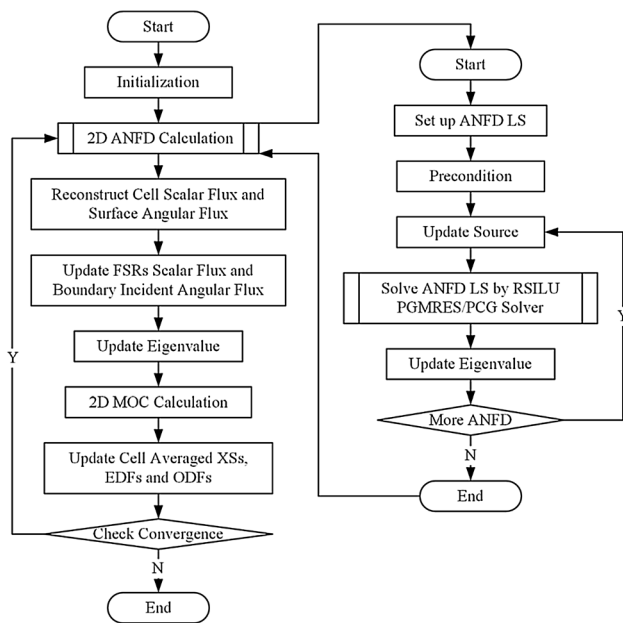


Fig. 2 Iteration scheme of ANFD method

$$AVG = \frac{\sum_N |e_n|}{N}, \tag{45a}$$

$$MAX = \max\{e_n\}, \tag{45b}$$

$$RMS = \frac{\sqrt{\sum_N e_n^2}}{N}, \tag{45c}$$

where e_n is the relative error of the even parity flux compared with that of the MOC solution, and N is the total number of even parity fluxes.

4.1 2D pin cell problem

As indicated in Fig. 3a, the side length of the cell was 1.26 cm, and the radius of the fuel pins was 0.54 cm for the 2D pin cell problem. The cross-sections data for the UO₂ fuel and moderator were obtained from the 2D C5G7 benchmark report. A vacuum boundary was applied to the east and south boundary surfaces, and the reflected boundary was applied to the north and west boundary surfaces. Three moderator rings and five fuel rings with 16 azimuthal divisions were selected for 128 flat-source regions.

For the 2D pin cell problem, Fig. 4a shows the angular distribution of the even parity flux in the first energy group, and Fig. 4b shows the energy group distribution of the even parity flux in the first azimuth angle. It is clear that the even parity flux distribution of the ANFD was consistent with the MOC solution in both the angle and energy groups. Table 1 shows the eigenvalue difference and overall even parity flux relative error. The difference in the eigenvalue was 0 pcm, and the flux maximum relative error was 3.683E−06.

4.2 2D assembly problem

As indicated in Fig. 3b, the 2D assembly problem comprised a 17 × 17 lattice of square pin cells containing a UO₂ fuel pin cell, guide tube, and fission chamber. The cross-sections data for these materials were obtained from the 2D C5G7 benchmark problem. The division of the flat-source region was the same as that of the 2D pin cell problem. As for the boundary conditions, vacuum boundary conditions were applied to the east and south boundary surfaces, whereas the reflected boundary conditions were applied to the north and west boundary surfaces.

Fig. 3 (Color online) Layout of 2D pin and 2D assembly problems

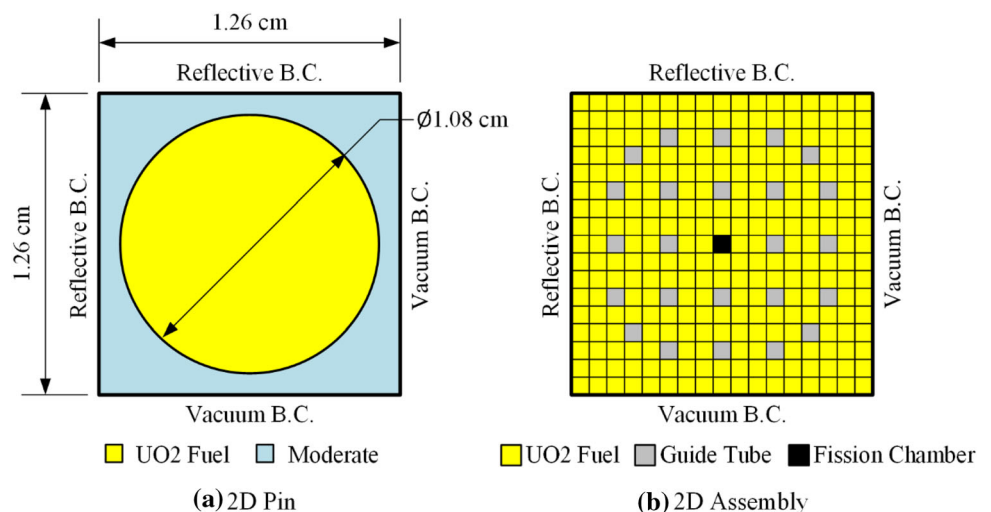


Fig. 4 (Color online) Normalized distribution of even parity flux in azimuth angle and energy group for 2D pin cell problem

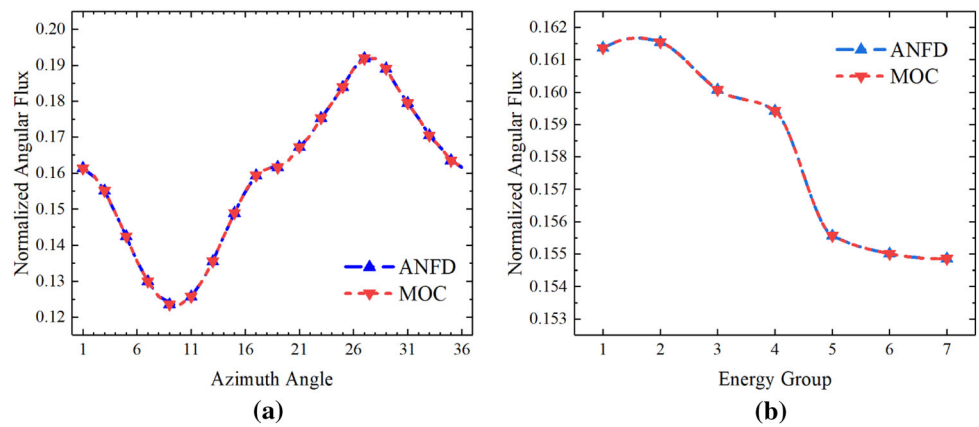


Table 1 Eigenvalue difference and even parity flux relative error for 2D pin cell problem

k_{eff}			Flux relative error		
MOC	ANFD	Error (pcm)	AVG	RMS	MAX
0.01561	0.01561	0	3.495E-07	9.145E-07	3.683E-06

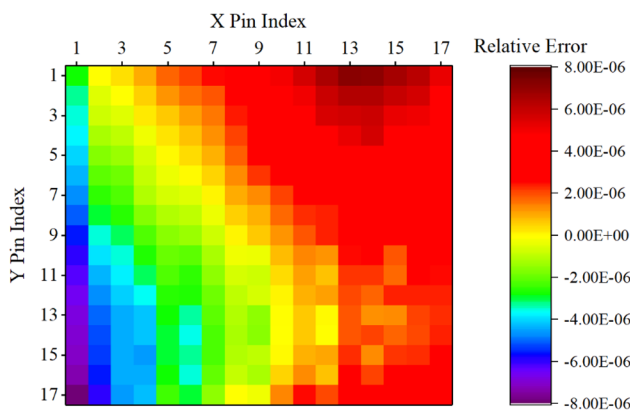


Fig. 5 (Color online) Even parity flux distribution relative error in first energy group and first azimuth angle for 2D assembly problem

Figure 5 shows the space relative error of the even parity flux in the first energy group and first azimuth angle for the 2D assembly problem. As shown, the even parity flux distribution of the ANFD indicated a relatively good agreement in space compared with the MOC solution. Table 2 shows the eigenvalue difference and overall even parity flux relative error for the 2D assembly problem. The difference in the eigenvalue was 0 pcm, whereas the flux maximum relative error was 1.162E-05.

4.3 2D C5G7 problem

The 2D C5G7 benchmark problem was originally a pin cell level heterogeneous benchmark for testing the accuracy of modern deterministic transport methods and codes without spatial homogenization. The 2D C5G7 problem

configuration is shown in Fig. 6. The overall geometry of this problem was 64.26 cm × 64.26 cm, and each assembly measured 21.42 cm × 21.42 cm. Each fuel assembly comprised a 17 × 17 lattice of square pin cells, including a moderator, guide tube, fission chamber, MOX fuel pin cell with different enrichment, and UO₂ fuel pin cell. For the reflector pin cases, the six additional pin cells of each reflector assembly used 1 × 1 sub mesh, whereas the 11 pin cells near the fuel used a 6 × 6 Cartesian sub mesh. For the other pin cells of the fuel and control rods, 128 flat-source regions comprising five fuel rings and three moderator rings with 16 azimuthal divisions were used. An accurate Monte-Carlo reference solution was provided in the 2D C5G7 benchmark report, which contains a precise eigenvalue solution and normalized pin power (NPP) that can be used as a reference solution. The NPP (p_r) in each fuel pin is defined as follows:

$$p_r = \frac{R_{f,r}}{\bar{R}_f}, \tag{46a}$$

$$R_{f,r} = \sum_{g=1}^G \Sigma_{f,g,r} \phi_{g,r} V_r, \tag{46b}$$

$$\bar{R}_f = \frac{\sum_{r=1}^N R_{f,r}}{N}, \tag{46c}$$

where $R_{f,r}$ is the fission rate in each fuel pin, \bar{R}_f the average fission rate of all fuel pins, and N the number of all fuel pins.

Figure 7 indicates the percent error of the NPP for the 2D C5G7 benchmark problem; as shown, the main error appeared in the fuel pin cell near the reflector.

Table 2 Eigenvalue difference and even parity flux relative error for 2D assembly problem

k_{eff}			Flux relative error		
MOC	ANFD	Error (pcm)	AVG	RMS	MAX
0.96848	0.96848	0	1.030E-06	1.742E-06	1.162E-05

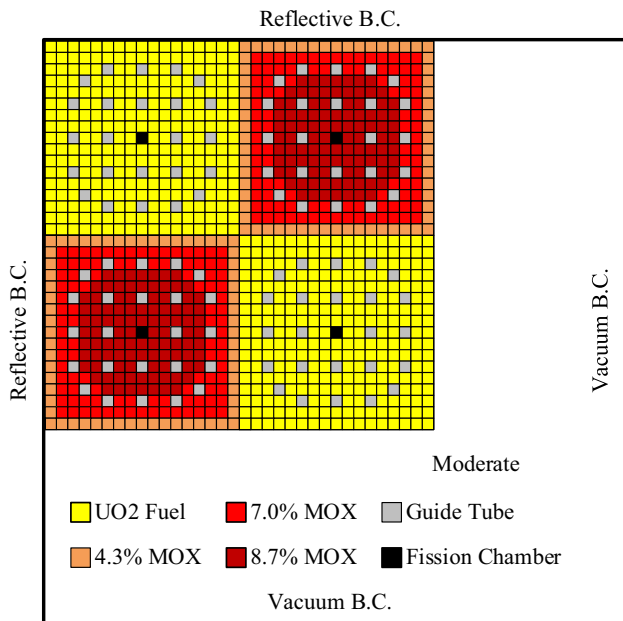


Fig. 6 (Color online) Layout of 2D C5G7 benchmark problem

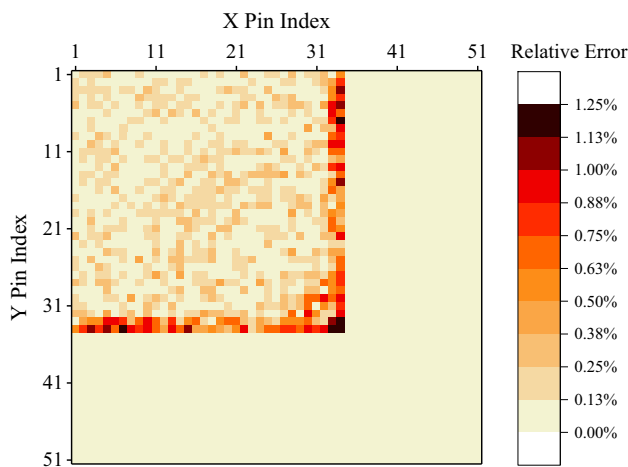


Fig. 7 (Color online) Percent error of pin power for 2D C5G7 benchmark problem

Table 3 shows the eigenvalue difference and NPP error from our results and the MCNP reference solutions. Compared with the reference results, the error of the eigenvalue was 3 pcm, which was less than the stochastic uncertainty of the MCNP reference results. In general, the

eigenvalue, NPP, etc., agreed well with the reference results.

4.4 Void region problem

The ANFD method was developed from transport theory and does not require the calculation of the diffusion coefficient. Therefore, the ANFD method may exhibit a better acceleration than the CMFD method in certain strongly anisotropic cases, such as those involving void regions and anisotropic scattering. In this study, a lattice problem involving void regions was constructed and tested; 5×5 square pin cells were set to the void regions, whereas UO₂ fuel cells were used in the other regions. The geometry and cross sections of the UO₂ fuel cell were the same as those provided in the 2D C5G7 benchmark report. The reflected boundary conditions were applied to all boundary surfaces. The layout of this void region problem is shown in Fig. 8.

The convergence history of the MOC, ANFD, and CMFD is shown in Table 4 and Fig. 9. As expected, the CMFD failed to converge in this problem, whereas the ANFD converged and remained effective.

Void regions are typical in real reactors, such as TREAT [27] and HTR-10 [28]. In a previous study [29], the quasi-diffusion method was used to address the void region problem in TREAT core analysis. In this study, the quasi-diffusion method was implemented using the nodal expansion method. Meanwhile, the nodal wise average cross sections, Eddington factors, and discontinuity factors were generated from 3D whole-core Serpent Monte-Carlo simulations. By comparison, the ANFD is more concise and only requires even and odd parity discontinuity factors generated from MOC calculations.

5 Conclusion

In this study, an innovative equivalent low-order ANFD method for MOC transport calculations was developed and implemented. The even parity discrete ordinates method was used to build a low-order ANFD equation, and different boundary condition treatments were proposed. Even and odd parity discontinuity factors based on the flux information obtained from MOC calculations were strictly defined to ensure the equivalence between this low-order equation and the high-order pin-resolved transport equation. The energy group and angle were decoupled to

Table 3 Eigenvalue and NPP data for 2D C5G7 benchmark problem

Parameters	Reference MCNP (Statistic error)	ANFD	Error
Eigenvalue			
k_{eff} (error/pcm)	1.18655 (\pm 9.5 pcm)	1.18652	-3 pcm
Specific NPP data			
Maximum NPP (error)	2.498 (\pm 0.16%)	2.494	- 0.14%
Minimum NPP (error)	0.232 (\pm 0.58%)	0.234	+ 1.04%
Normalized assembly power data			
Inner UO ₂ power (error)	492.8 (\pm 0.10%)	492.3	- 0.10%
MOX power (error)	211.7 (\pm 0.18%)	211.9	+ 0.10%
Outer UO ₂ power (error)	139.8 (\pm 0.20%)	139.9	+ 0.10%
NPP error results			
MAX error	-	1.25%	-
AVG error	0.32%	0.21%	-
RMS error	0.34%	0.30%	-
MRE error	0.27%	0.16%	-

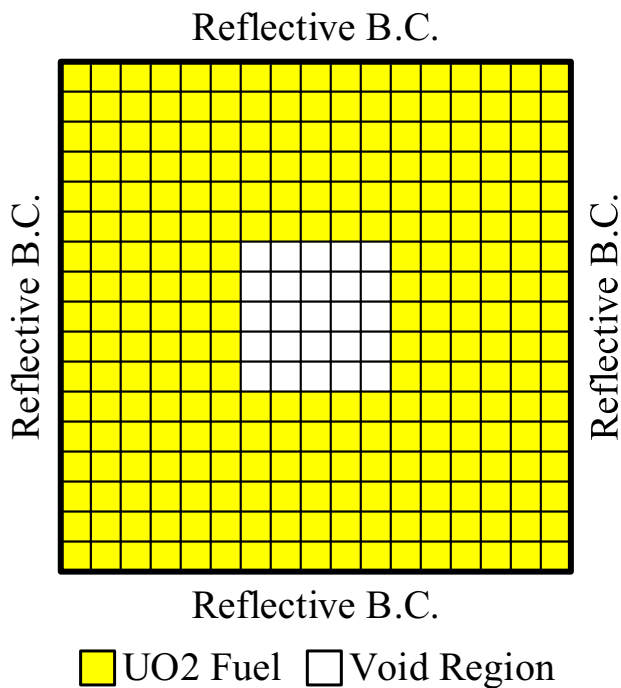


Fig. 8 (Color online) Layout of lattice case involving void regions

construct an easier-to-solve symmetric linear system. The self-developed RSILU preconditioned GMRES solver was applied to solve this linear system. The equivalence of the ANFD method was verified for 2D pin, 2D assembly, and 2D C5G7 benchmark problems. The numerical results

Table 4 Acceleration performances of ANFD and CMFD

	k_{eff}	Error	MOC iteration number	Speedup
No acceleration	1.32592	-	91	-
CMFD	Divergence	-	-	-
ANFD	1.32602	10 pcm	11	8.3

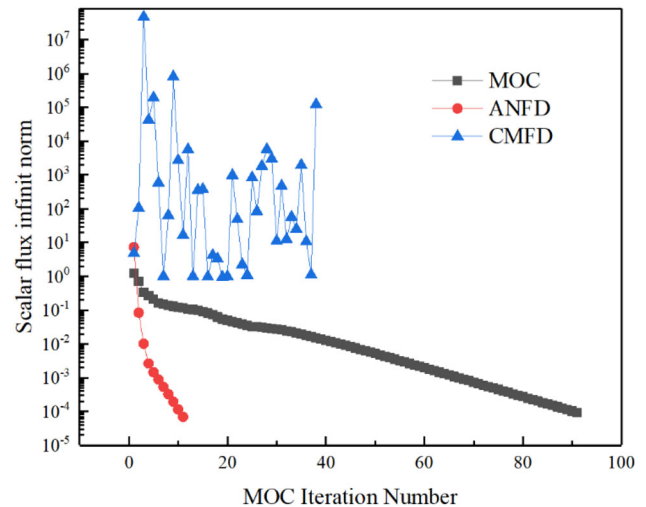


Fig. 9 (Color online) Convergence histories of MOC, ANFD, and CMFD

demonstrated that a low-order ANFD equation that was completely equivalent to the pin-resolved transport equation was established.

This study provides an important foundation for further developing a novel acceleration technique based on the ANFD method. Only an equivalent equation was established, and a converged consistent solution was obtained to achieve acceleration. In the future, the acceleration performance of the ANFD will be tested. Meanwhile, we will compare the pin-homogenized ANFD method with the pin-

homogenized MG CMFD method, which is widely used to accelerate MOC calculations. Our preliminary analysis indicated that the ANFD method achieved an excellent and stable acceleration performance compared with the CMFD method when void regions existed. Other anisotropic cases, such as anisotropic scattering, will be tested in our future studies. Subsequently, Fourier analysis will be used for convergence analysis. Additionally, we will investigate the use of the multilevel acceleration method to reduce the computing burden of ANFD and then attempt to extend this method to 3D cases.

References

- N.Z. Cho, G.S. Lee, C.J. Park, Fusion of method of characteristics and nodal method for 3-d whole-core transport calculation. *Trans. Am. Nucl. Soc.* **87**, 322 (2002)
- H. G. Joo, J. Y. Cho, K. S. Kim et al, Methods and performance of a three dimensional whole-core transport code DeCART. *PHYSOR 2004—The Physics of Fuel Cycles and Advanced Nuclear Systems*, Chicago, Illinois, US. (2004)
- J.Y. Cho, H.G. Joo, Solution of the C5G7MOX benchmark three-dimensional extension problems by the DeCART direct whole core calculation code. *Prog. Nucl. Energy* **48**, 456 (2006). <https://doi.org/10.1016/j.pnucene.2006.01.006>
- Y.S. Jung, C.B. Shim, C.H. Lim et al., Practical numerical reactor employing direct whole core neutron transport and subchannel thermal/hydraulic solvers. *Ann. Nucl. Energy* **62**, 357 (2013). <https://doi.org/10.1016/j.anucene.2013.06.031>
- B. Collins, S. Stimpson, B.W. Kelley et al., Stability and accuracy of 3D neutron transport simulations using the 2D/1D method in MPACT. *J. Comput. Phys.* **326**, 612 (2016). <https://doi.org/10.1016/j.jcp.2016.08.022>
- Z. Liu, L. Liang, J. Chen et al., Accuracy and analysis of the iteratively coupling 2D/3D method for the three-dimensional transport calculations. *Ann. Nucl. Energy* **113**, 130 (2018). <https://doi.org/10.1016/j.anucene.2017.10.020>
- J. Choe, S. Choi, P. Zhang et al., Verification and validation of STREAM/RASTK for PWR analysis. *Nucl. Eng. Tech.* **51**(2), 356 (2019). <https://doi.org/10.1016/j.net.2018.10.004>
- K. S. Smith. *Spatial Homogenization Methods for Light Water Reactors*. Doctoral thesis, Massachusetts Institute of Technology (1980).
- A. Zhu, M. Jarrett, Y. Xu et al., An optimally diffusive coarse mesh finite difference method to accelerate neutron transport calculations. *Ann. Nucl. Energy* **95**, 116 (2016). <https://doi.org/10.1016/j.anucene.2016.05.004>
- S. Yuk, N.Z. Cho, Two-level convergence speedup schemes for p-CMFD acceleration in neutron transport calculation. *Nucl. Sci. Eng.* **188**, 1 (2017). <https://doi.org/10.1080/00295639.2017.1332891>
- Y. Xu, T. J. Downar, Convergence Analysis of a CMFD Method Based on Generalized Equivalence Theory. *PHYSOR 2012*, Knoxville, Tennessee, April 15–20. (2012)
- D. Wang, S. Xiao, A linear prolongation approach to stabilizing CMFD. *Nucl. Sci. Eng.* **190**, 45 (2018). <https://doi.org/10.1080/00295639.2017.1417347>
- X. Chai, D. Yao, K. Wang et al., Generalized coarse-mesh finite difference acceleration for method of characteristics in unstructured meshes. *Chin. J. Comput. Phys.* **27**(4), 541 (2010)
- C. Hao, L. Kang, Y. Xu et al., 3D whole-core neutron transport simulation using 2D/1D method via multi-level generalized equivalence theory based CMFD acceleration. *Ann. Nucl. Energy* **122**, 79 (2018). <https://doi.org/10.1016/j.anucene.2018.08.014>
- Z. Liu, X. Zhou, L. Cao et al., A new three-level CMFD method based on the loosely coupled parallel strategy. *Ann. Nucl. Energy* **145**, 107529 (2020). <https://doi.org/10.1016/j.anucene.2020.107529>
- L. Kang, C. Hao, Q. Zhao et al., Two-level time-dependent GET based CMFD acceleration for 3D whole core transient transport simulation using 2D/1D method. *Ann. Nucl. Energy* **142**, 107405 (2020). <https://doi.org/10.1016/j.anucene.2020.107405>
- A. Zhu. *Transient methods for pin-resolved whole-core neutron transport*. Doctoral thesis, The University of Michigan (2016).
- M. Jarrett, B. Kochunas, A. Zhu, et al., Analysis of stabilization techniques for CMFD acceleration of neutron transport problems. *Nucl. Sci. Eng.* **184**, 208 (2016). <https://doi.org/10.13182/NSE16-51>
- Q. Shen, Y. Xu, T. Downar, Stability analysis of the CMFD scheme with linear prolongation. *Ann. Nucl. Energy* **129**, 298 (2019). <https://doi.org/10.1016/j.anucene.2019.02.011>
- M.A. Smith, E.E. Lewis, C.B. Na, Benchmark on deterministic 2-D MOX fuel assembly transport calculations without spatial homogenization. *Prog. Nucl. Energy* **45**, 107 (2004). <https://doi.org/10.1016/j.pnucene.2004.09.003>
- Y. Saad, *Iteration Methods for Sparse Linear Systems* (PWS Publishing Company, Boston, 1996), pp. 245–247
- C. Hao, Y. Xu, T. Downar, Multi-level coarse mesh finite difference acceleration with local two-node nodal expansion method. *Ann. Nucl. Energy* **116**, 105 (2018). <https://doi.org/10.1016/j.anucene.2018.02.002>
- J.I. Yoon, H.G. Joo, Two-level coarse mesh finite difference formulation with multigroup source expansion nodal kernels. *J. Nucl. Sci. Technol.* **45**, 668 (2008)
- Z. Zhong, T. Downar, Y. Xu, et al., Implementation of two-level coarse-mesh finite difference acceleration in an arbitrary geometry, two-dimensional discrete ordinates transport method. *Nucl. Sci. Eng.* **158** (3), 289 (2008). <https://doi.org/10.13182/NSE06-24TN>
- Y. Xu, C. Hao, A novel and efficient hybrid RSILU preconditioner for the parallel GMRES solution of the coarse mesh finite difference equations for practical reactor simulations. *Nucl. Sci. Eng.* **194**(2), 104 (2019). <https://doi.org/10.1080/00295639.2019.1657322>
- A. Yamamoto, M. Tabuchi, N. Sugimura et al., Derivation of optimum polar angle quadrature set for the method of characteristics based on approximation error for the Bickley function. *J. Nucl. Sci. Technol.* **44**(2), 129 (2007). <https://doi.org/10.1080/18811248.2007.9711266>
- G.A. Freund, P. Elias, D. R. MacFarlane, J. D. Geier, J.F. Boland, Design Summary Report on the Transient Reactor Test Facility (TREAT), ANL-6034, Argonne National Laboratory, (1960).
- Z. Wu, D. Lin, D. Zhong, The design features of the HTR-10. *Nucl. Eng. Des.* **218**(3), 25 (2002). [https://doi.org/10.1016/S0029-5493\(02\)00182-6](https://doi.org/10.1016/S0029-5493(02)00182-6)
- Y. Xu, V. Seker, T. Downar, Quasi-diffusion method with 3-D cross sections for TREAT core analysis. *Nucl. Technol.* **206**(6), 825 (2020). <https://doi.org/10.1080/00295450.2019.1672451>